

Physics-embedded machine learning search for Sm-doped PMN-PT piezoelectric ceramics with high performance

Rui Xin(辛睿), Yaqi Wang(王亚祺), Ze Fang(房泽), Fengji Zheng(郑凤基), Wen Gao(高雯), Dashi Fu(付大石), Guoqing Shi(史国庆), Jian-Yi Liu(刘建一), and Yongcheng Zhang(张永成)
Citation: Chin. Phys. B, 2024, 33 (**8**): 087701. DOI: 10.1088/1674-1056/ad51f3

What follows is a list of articles you may be interested in

CuO added $Pb_{0.92}Sr_{0.06}Ba_{0.02}(Mg_{1/3}Nb_{2/3})_{0.25}(Ti_{0.53}Zr_{0.47})_{0.75}O_3$ ceramics sintered with Ag electrodes at 900℃ for multilayer piezoelectric actuator

Muhammad Adnan Qaiser, Ahmad Hussain, Yuqing Xu(徐玉青), Yaojin Wang(汪尧进), Yiping Wang(王一平), Ying Yang(杨颖), Guoliang Yuan(袁国亮)
Chin. Phys. B, 2017, 26 (**3**): 037702. DOI: 10.1088/1674-1056/26/3/037702

Dielectric and piezoelectric properties of (110) oriented $Pb(Zr_{1-x}Ti_x)O_3$ thin films

Jian-Hua Qiu(邱建华), Zhi-Hui Chen(陈智慧), Xiu-Qin Wang(王秀琴), Ning-Yi Yuan(袁宁一), Jian-Ning Ding(丁建宁)
Chin. Phys. B, 2016, 25 (**5**): 057701. DOI: 10.1088/1674-1056/25/5/057701

Preparation and characterization of $Sr_{0.5}Ba_{0.5}Nb_2O_6$ glass-ceramic on piezoelectric properties

Shan Jiang(姜珊), Xuan-Ming Wang(王炫明), Jia-Yu Li(李佳宇),Yong Zhang(张勇), Tao Zheng(郑涛), Jing-Wen Lv(吕景文)
Chin. Phys. B, 2016, 25 (**3**): 037701. DOI: 10.1088/1674-1056/25/3/037701

Piezoelectric and electro—optic properties of tetragonal $(1-x)Pb(Mg_{1/3}Nb_{2/3})O_3$—$xPbTiO_3$ single crystals by phenomenological theory

Qiu Jian-Hua (邱建华), Wang Xiu-Qin (王秀琴), Yuan Ning-Yi (袁宁一), Ding Jian-Ning (丁建宁)
Chin. Phys. B, 2015, 24 (**7**): 077701. DOI: 10.1088/1674-1056/24/7/077701

Preparation and piezoelectric properties of potassium sodium niobate glass ceramics

Jiang Shan (姜珊), Wang Xuan-Ming (王炫明), Li Jia-Yu (李佳宇), Zhang Yong (张勇), Zheng Tao (郑涛), Lv Jing-Wen (吕景文)
Chin. Phys. B, 2015, 24 (**6**): 067701. DOI: 10.1088/1674-1056/24/6/067701

DATA PAPER

Physics-embedded machine learning search for Sm-doped PMN-PT piezoelectric ceramics with high performance

Rui Xin(辛睿)[1], Yaqi Wang(王亚祺)[1], Ze Fang(房泽)[1], Fengji Zheng(郑凤基)[1], Wen Gao(高雯)[1], Dashi Fu(付大石)[1], Guoqing Shi(史国庆)[1], Jian-Yi Liu(刘建一)[1,2,†], and Yongcheng Zhang(张永成)[1,‡]

[1] *College of Physics, Center for Marine Observation and Communications, National Demonstration Center for Experimental Applied Physics Education, Qingdao University, Qingdao* 266071, *China*

[2] *Centre for Theoretical and Computational Physics, College of Physics, Qingdao University, Qingdao* 266071, *China*

(Received 3 February 2024; revised manuscript received 23 May 2024; accepted manuscript online 30 May 2024)

$Pb(Mg_{1/3}Nb_{2/3})O_3$–$PbTiO_3$ (PMN-PT) piezoelectric ceramics have excellent piezoelectric properties and are used in a wide range of applications. Adjusting the solid solution ratios of PMN/PT and different concentrations of elemental doping are the main methods to modulate their piezoelectric coefficients. The combination of these controllable conditions leads to an exponential increase of possible compositions in ceramics, which makes it not easy to extend the sample data by additional experimental or theoretical calculations. In this paper, a physics-embedded machine learning method is proposed to overcome the difficulties in obtaining piezoelectric coefficients and Curie temperatures of Sm-doped PMN-PT ceramics with different components. In contrast to all-data-driven model, physics-embedded machine learning is able to learn nonlinear variation rules based on small datasets through potential correlation between ferroelectric properties. Based on the model outputs, the positions of morphotropic phase boundary (MPB) with different Sm doping amounts are explored. We also find the components with the best piezoelectric property and comprehensive performance. Moreover, we set up a database according to the obtained results, through which we can quickly find the optimal components of Sm-doped PMN-PT ceramics according to our specific needs.

Keywords: $Pb(Mg_{1/3}Nb_{2/3})O_3$–$PbTiO_3$ (PMN-PT) ceramic, physics-embedded machine learning, piezoelectric coefficient, Curie temperature

PACS: 77.84.–s, 77.84.Cg, 77.90.+k, 77.80.Jk **DOI:** 10.1088/1674-1056/ad51f3

1. Introduction

Piezoelectric ceramics have long been of interest to both fundamental research and industrial production due to the wide range of applications[1–3] and the advantages of short preparation cycles, low production costs, and greater suitability for industrial production compared to single crystals.[4] Among them, $Pb(Mg_{1/3}Nb_{2/3})O_3$–$PbTiO_3$ (PMN-PT) piezoelectric ceramics, which have excellent piezoelectric properties, are the focus of current research.[5–7] Recently, a large number of theoretical and experimental investigations have been carried out mostly on piezoelectric coefficients in order to expand the range of potential applications. To the best of our knowledge, there are two underlying mechanisms in theory that play important roles in determining the piezoelectric coefficient. The first is that the piezoelectric coefficient increases dramatically as the material components approach the morphotropic phase boundary (MPB).[8] The other one is that piezoelectric properties can be further enhanced by introducing nanoscale structural heterogeneity through rare earth element doping.[9] Guided by theory, experimentally reported piezoelectric coefficients of PMN-PT-based ceramics continue to break new heights. For example, the researchers prepared PMN-PT-based piezoelectric ceramics with d_{33} up to 1420 pC/N by doping Eu.[10] At the same time, PMN-PT-based piezoelectric ceramics with d_{33} up to 1510 pC/N[9] and 1406 pC/N[11] have also been experimentally obtained by doping Sm.

Based on the results of existing research, two difficulties encountered so far are summarized here. Firstly, there is a mutual restriction between piezoelectric coefficient and Curie temperature. That is to say, when Curie temperature (T_c) changes, d_{33} usually changes in the opposite direction, and vice versa. For example, the T_c of Sm-doped PMN-PT ceramic with d_{33} being 1510 pC/N is reported to be only about 89 °C, while the T_c of Sm-doped PMN-PT ceramic with d_{33} being about 700 pC/N is as high as 157 °C. Secondly, compared with undoped ceramics, element doped-PMN-PT-based piezoelectric ceramics have more possible components, so the workload required to experimentally screen materials with suitable compositions becomes very large. Therefore, how to find the specific composition PMN-PT ceramics with high performance (high d_{33} and T_c) is a core issue. In general, theoretical calculations, such as phase field simulations which have achieved many important results,[12–14] are expected to play important

†Corresponding author. E-mail: jianyi_liu@qdu.edu.cn
‡Corresponding author. E-mail: qdzhyc@qdu.edu.cn

© 2024 Chinese Physical Society and IOP Publishing Ltd

roles in the search for targeted high-performance piezoelectric ceramic materials. Nevertheless, due to the complex structure of ceramics, simulating ceramic materials through theoretical modeling is not a simple task. In contrast, theoretical simulations are currently used more on single-crystal materials.[15] Therefore, it still mostly relies on experimental research to prepare PMN-PT ceramics with various element doping and compositions to find conditions for high performance, which will bring a huge workload.

In recent years, machine learning has been increasingly applied to guide the development and synthesis of new materials.[16] For example, machine learning was combined with feature engineering to realize the search for $BaTiO_3$-based ceramics with large piezoelectric coefficient and large energy storage capacity at low fields.[17–19] Machine learning techniques can learn the rules behind a data set by evaluating a portion of the data and building models to make predictions. This makes it well suited to the problem of probing material properties. However, machine learning encounters difficulties in predicting the piezoelectric coefficients of Sm-doped PMN-PT ceramics with different components. This is due to the fact that the variation of piezoelectric coefficients is nonlinear, and it is difficult for polynomial regression models to accurately learn variation rules. Some new models with better performance obtain the ability to learn nonlinear variation rules, but this type of all-data-driven model requires a large amount of data for training. The data obtained experimentally is often insufficient. Many researches have been done on the small data material problem.[20] Here, we introduce physics-embedded machine learning[21] to solve this problem. Compared to all-data-driven machine learning that takes a purely data-driven approach, physics-embedded machine learning is driven by both knowledge and data,[22] significantly reducing the number of samples required. In this way, we can train a physics-embedded machine learning model to accurately predict nonlinearly varying piezoelectric coefficients based on small datasets.

In this study, we train a physics-embedded machine learning model instead of all-data-driven model according to published experimental results.[9] Our model successfully overcomes the difficulties of predicting nonlinearly varying piezoelectric coefficients based on small datasets. Since Sm doping enhances the piezoelectric properties of PMN-PT ceramics more significantly compared to other elements,[23] we obtain the piezoelectric coefficient and Curie temperature of Sm-doped PMN-PT piezoelectric ceramics with very detailed components using our model. Through this result, all the MPB positions of Sm-doped PMN-PT ceramics with different doping amounts are explored. We also find the components with the best piezoelectric property and comprehensive performance. Moreover, we set up a database from the results obtained, through which we can quickly find the optimal components of Sm-doped PMN-PT ceramics according to our specific needs.

2. Method

2.1. Workflow of machine learning

The workflow of machine learning is shown in Fig. 1(a) and the structure of the physics-embedded model is shown in Fig. 1(b). Since we wish to establish a correlation from material components to d_{33}, the inputs to the model are the solid solution ratios of PMN/PT and the doping amount of Sm. The physics-embedded machine learning model is divided into three parts, the first part predicts each of the intermediate variables based on the model inputs. Intermediate variables need to be set based on physics knowledge, which is the most central part of physics-embedded machine learning. It was mentioned that T_c and d_{33} have strong mutual constraints,[24] so we choose T_c as one of the intermediate variables. According to the formula $d_{33} = 2\varepsilon P_s Q_m$,[9] the dielectric permittivity (ε)[25] is added to the intermediate variables. Constrained by the experimental data, we abandon the electrostrictive coefficient (Q_m) and use remnant polarization (P_r)[26] and coercive field (E_c)[27] to model the role of spontaneous polarization (P_s). Microstructures such as the grain boundaries, the order of grain orientation and domain structures, etc. play important roles in determining the properties of piezoelectric ceramic materials,[28] and it is very important to investigate the effects of the above microstructures in the long term. To consider such factors in the machine learning model, we need enough experimental data to summarize the key information in the microstructure. However, our work is based on publicly available experimental datasets, so we do not have access to detailed information about the microstructure. On the other hand, the minimum energy of the system corresponds to a random grain orientation[9,29] and most of the doped Sm is in the lattice of the grains, which does not change the grain orientation or boundaries. Since the model is to study PMN-PT ceramics doped with different concentrations of Sm, grain orientations and boundaries are not considered. The second part uses the activation function[30] to deal with the intermediate variables obtained in the first part, which gives the whole model the ability to learn nonlinear patterns of change. Finally, the results can be obtained based on the activated intermediate variables. The models for each step of prediction are trained on experimental data. Limited by the sample size, all predictions are realized by polynomial regression.

Another problem brought by small datasets is that chance results may occur when verifying the accuracy of the model, thus reducing the credibility of the validation results. To solve this problem, we adopt a K-fold cross validation[31] approach

to test the model, as shown in Fig. 1(c). Firstly, the samples are equally divided into several groups, one of which is selected as the test set for validation, and the other data are used to train the model. Then, each set of data is rotated as a test set and the above operation is repeated. In this way, we avoid the limitations and peculiarities of a fixed division of the data sets, and can reduce the risk of model overfitting.[32] It also greatly avoids the occurrence of chance result.

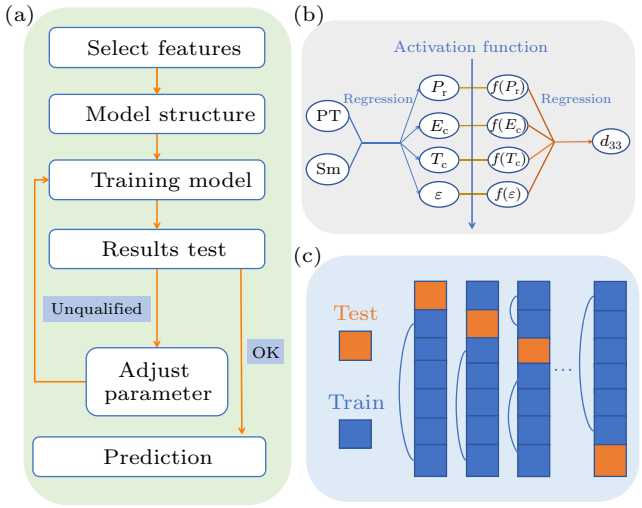


Fig. 1. Schematic of the machine learning approach in this paper. (a) Workflow of machine learning. (b) Physics-embedded machine learning model structure. (c) K-fold cross validation.

2.2. Validation of results

In order to be able to quantitatively compare the differences in the accuracy of the predictions of different models, we select the three most commonly used evaluation metrics in machine learning, which are R^2_{score},[33] root mean square error[34] (RMSE) and mean absolute error[35] (MAE). The formulas are as follows:

$$R^2_{\text{score}} = 1 - \frac{\sum_{i=1}^{n}(y_i - \hat{y}_i)^2}{\sum_{i=1}^{n}(y_i - \bar{y})^2}, \tag{1}$$

$$\text{MAE} = \frac{1}{n}\sum_{i=1}^{n}|y_i - \hat{y}_i|, \tag{2}$$

$$\text{RMSE} = \sqrt{\frac{1}{n}\sum_{i=1}^{n}(y_i - \hat{y}_i)^2}, \tag{3}$$

where y_i is the true value of the sample, $\hat{y}_i$ is the predicted value of the sample, and $\bar{y}$ is the mean of the true values. Table 1 shows the prediction accuracies of different degrees in each step of the polynomial regression, as measured by R^2_{score}. It can be seen that choosing the right polynomial regression degree has a very strong impact on the prediction results. In general, the degree of polynomial regression should not be excessive. Otherwise, it is easy to make the model overfitting, which leads to the accuracy decrease.

Table 2 shows the validation results for the intermediate variables. As can be seen from the data in the table, for the Curie temperature, the model has an amazing R^2_{score} of 0.99, and the RMSE and MAE are 2.66 and 2.16, respectively, which proves that the prediction results are very accurate. Meanwhile, according to the evaluation metrics, it can be seen that the model also predicts the results accurately for the other three parameters.

In order to verify the reasonableness of the intermediate variables set up in this paper through prior knowledge, Table 3 gives the changes in model performance after removing any one of the parameters. From the data, the effect of removing any of the ferroelectric properties is not as great as the dielectric constant. This may be due to the fact that there is still some correlation between the ferroelectric properties, and the effects of the deleted parameters can be compensated for by the remaining parameters, while dielectric constants do not have such a compensation mechanism.

Table 1. The R^2_{score} of polynomial regression with different degrees.

Predicted target	Degree = 1	Degree = 2	Degree = 3	Degree = 4
T_c	0.98	0.96	0.99	0.76
ε	−0.18	0.77	0.43	0.4
P_r	0.68	0.65	0.82	0.65
E_c	0.88	0.8	0.65	−0.6
d_{33}	0.91	0.8	0.21	0.52

Table 2. Validation of intermediate variables.

Parameters	R^2_{score}	RMSE	MAE
T_c	0.99	2.66	2.16
ε	0.77	1811	1374
P_r	0.82	0.99	0.85
E_c	0.88	0.35	0.27

Table 3. Performance variations of the physics-embedded model.

Model	R^2_{score}	RMSE	MAE
All-inclusive	0.91	98.3	80.8
Ignore T_c	0.90	100.6	83.9
Ignore ε	−0.16	295.8	252.1
Ignore P_r	0.90	99.3	76.4
Ignore E_c	0.88	113.2	97.2

Next, we will compare the performance of physics-embedded model and all-data-driven model. Due to the limitation of the sample size, only a polynomial regression model directly from material components to piezoelectric coefficients can be chosen to represent all-data-driven models. Figure 2(a) shows the evaluation parameters of the physics-embedded machine learning model and the all-data-driven model. As can be seen from Fig. 2(a), there is a significant improvement in the performance of the physics-embedded model compared with all-data-driven model. R^2_{score} is improved from 0.71 to 0.91, and RMSE and MAE are reduced by about half. In order to compare the predictions of the two models for each specific sample, we plot Fig. 2(b) based on the available data. In

Fig. 2(b), the height of the columns means how much larger the all-data-driven model's error is than the physics-embedded model. If the columns are downward, it means that the error of the physics-embedded model is larger. Apparently, almost all of the columns are upward and much higher than the downward ones. This proves that the model in this paper is more accurate in predicting the vast majority of the samples.

To visually compare the performance of the two models, we validate both models with a series of visualizations. Figures 2(c) and 2(d) show the visualized regression results for both models. The horizontal axis represents the true value of the sample and the vertical axis represents the predicted value of the model for that sample. That means that the closer the coordinate point corresponding to each sample is to the line $y = x$, the more accurate the model's prediction of that sample will be. When the coordinate points are on the line $y = x$, the prediction is exactly equal to the true value. The line $y = x$ is labeled for easy observation. Obviously, the predicted results of the physics-embedded model fit the regression line much better, while the all-data-driven model even deviates from the regression line at some points. This proves that the method proposed in this paper is even better.

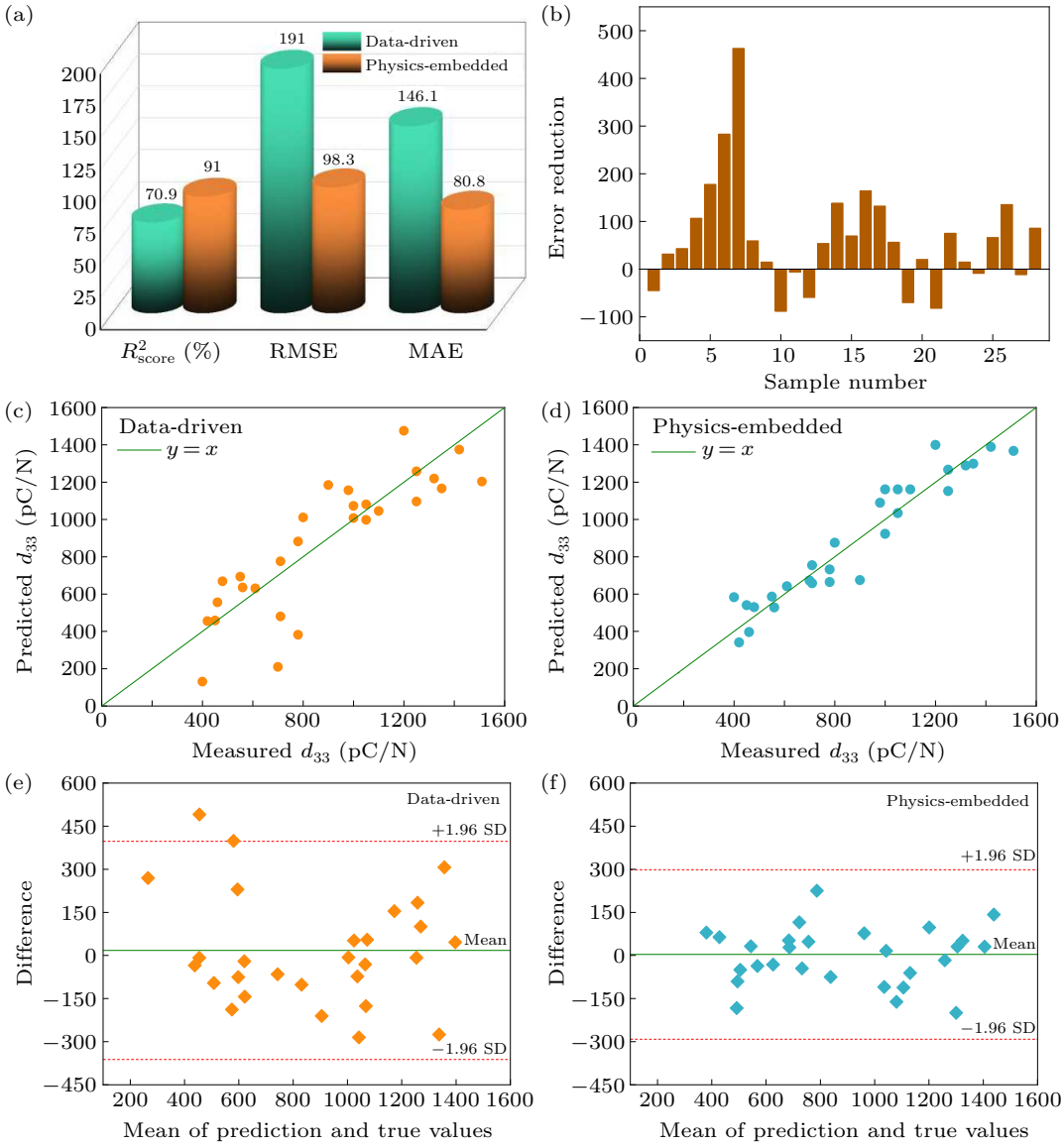


Fig. 2. Validation results of the models. (a) Evaluation parameters of all-data-driven model and the physics-embedded model, including R^2_{score}, RMSE and MAE. (b) Error reduction of physics-embedded model over all-data-driven model on each sample. Visualization of predicted results for all-data-driven models (c) and the physics-embedded model (d). Bland–Altman validation of all-data-driven model (e) and the physics-embedded model (f).

Figures 2(e) and 2(f) show the Bland–Altman plots[36,37] of the predictions of both models. In machine learning, Bland–Altman analysis can be used to assess whether there is good agreement between predicted and true values. The horizontal axis of the graph represents the mean of the true and predicted values, and the vertical axis represents the difference between the true and predicted values. The mean of all differences is d (the green solid line), and the standard devia-

tion of all differences from d is S_d. If the distribution of the differences follows a normal distribution,[38] 95% of the differences should lie between $d - 1.96S_d$ and $d + 1.96S_d$ (the red dotted line). If the difference between the two sets of values is almost exactly within the range, this indicates that they are in good agreement and that the machine learning predictions reflect the true values well. All the differences of the physics-embedded model are within range and more convergent. In addition, the mean difference and standard deviation of the physics-embedded model are also smaller than those of the all-data-driven model, which indicates that our model is better.

Table 4. Experimental validation results of Sm-doped 0.7PMN–0.3PT.

Sm concentration (mol%)	Experimental d_{33} (pC/N)	Predicted d_{33} (pC/N)
1	569	602.13
2	1018	1128.26
2.5	1406	1243.07
3	1287	1203.91

However, validation methods for the prediction results are limited to the dataset only, which is insufficient. Therefore, the model is validated again with experimental data from another process. The experimental data used are d_{33} of 0.7PMN–0.3PT ceramics with different Sm doping concentrations[11] and the results of the experimental validation are recorded in Table 4. Although there are few differences in the preparation process, the results predicted by the model are still consistent with the experiments (MAE = 97.4). And the variation rules of piezoelectric performance for different components are also matched. The reliability of the model in this paper is further confirmed by experimental validation.

3. Results and discussion

3.1. MPB positions with different Sm doping amounts

Since Sm doping enhances the piezoelectric properties of PMN-PT ceramics more significantly compared to other elements according to available literature,[23] we focus on Sm-doped PMN-PT ceramics attempting to figure out the rules for the variation of d_{33} and T_c with components. Firstly, we predict the d_{33} and T_c of Sm-doped PMN-PT ceramics at detailed components by the model designed in this paper. Then we try to find the exact location where the MPB piezoelectric peak appears based on the above data. The predicted results of d_{33} as a function of PT content at different Sm doping amounts are shown in Fig. 3. The data in light blue in Fig. 3 represents that its PT content lies in the interval for which no experimental data are available and is extended by machine learning. The orange dotted line marks the locations of the MPB peaks. Through Fig. 3 we can learn that with increasing Sm doping amount, the position of MPB moves in the direction of decreasing content of PT. The reason for this phenomenon may be that elemental doping changes the electronic structure and lattice constants of the material, thus affecting the stability and position of the phase boundaries.[39] In addition, the speed of MPB position changing slows down with the increase of Sm doping amount. When the Sm doping amount reaches about 2.5 mol%, the position of MPB no longer moves and stays around PMN–28.4%PT.

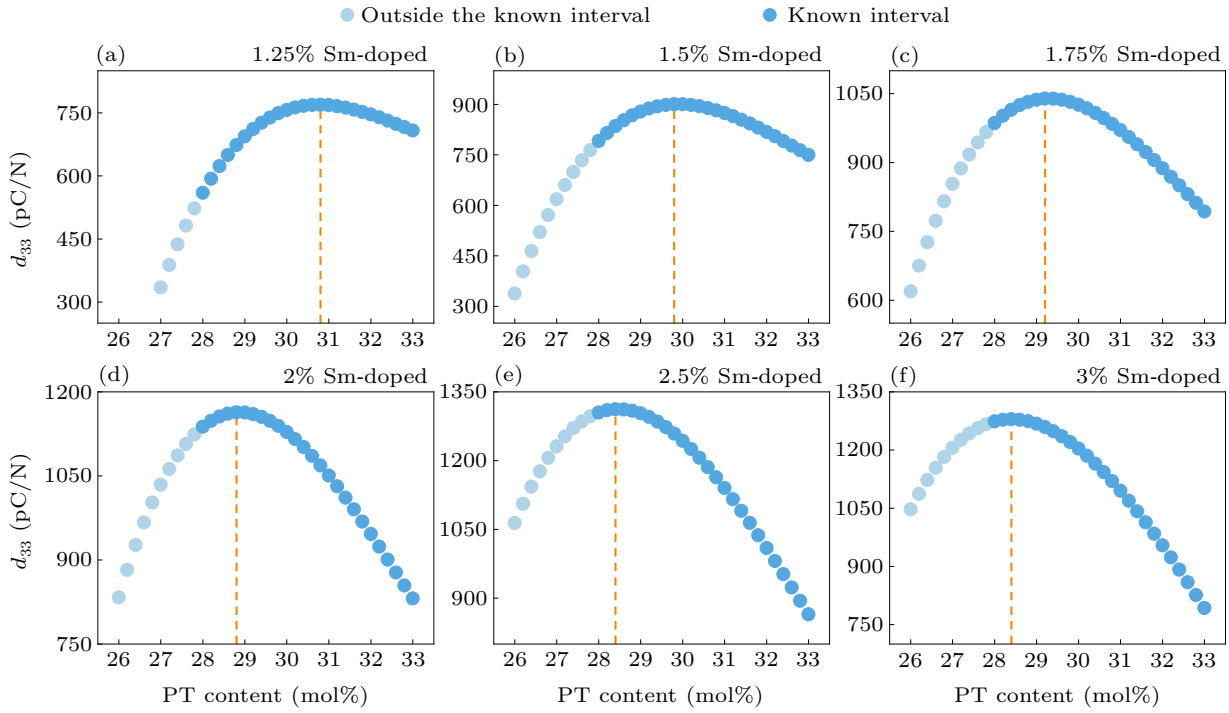


Fig. 3. Locations of MPB piezoelectric peaks in PMN-PT ceramics at (a)–(f) 1.25 mol%, 1.5 mol%, 1.75 mol%, 2 mol%, 2.5 mol%, 3 mol% Sm doping.

3.2. Comprehensive performance at MPB

As mentioned earlier, piezoelectric coefficient and Curie temperature are the two most important properties of piezoelectric materials. In the following, we discuss the comprehensive performance of ceramics at the MPB based on the results obtained above. Figure 4 shows the d_{33} and T_c at MPB for PMN-PT ceramics with different Sm doping amounts. The darker green color in the graph means that the piezoelectric coefficient is larger. It is clear that the maximum piezoelectric coefficient (about 1321 pC/N) is achieved at 2.75 mol% Sm doping when Curie temperature is not considered. The reason that this value is smaller than the maximum value of the experiment we consider to be due to the model needs to learn the rules of variation of the data, and the extreme sample values must be close to the average value. In the predictions of the model, the performance of this component is higher than the component which achieves the maximum value in the experiments. From a comprehensive performance point of view, the piezoelectric coefficient increases faster and then slower with increasing Sm doping. At the same time, the Curie temperature is dropping slower and slower. When the Sm doping amount exceeds 2.75 mol%, the piezoelectric coefficient turns to decrease, while T_c decreases sharply. In conclusion, we believe that both 2.5 mol% Sm and 2.75 mol% Sm-doped ceramics have good comprehensive performance at MPB.

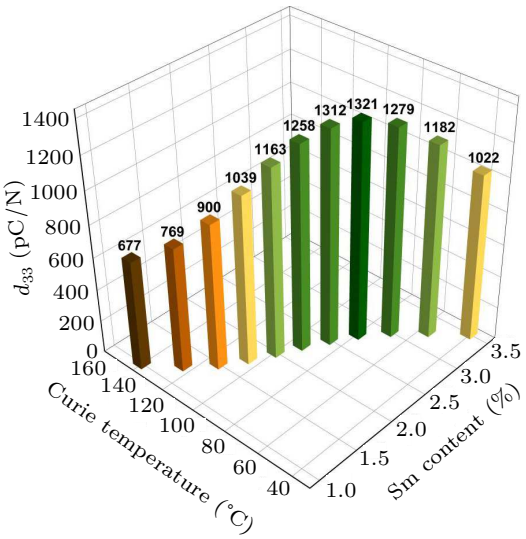


Fig. 4. The T_c and d_{33} at MPB of PMN-PT ceramics with different Sm doping amounts.

3.3. Factors affecting piezoelectric coefficients at MPB

In the following, we attempt to explore the mechanisms underlying the trends in d_{33} at MPB. To do so, we plot the variation of d_{33} with P_r, E_c, ε at MPB positions in Fig. 5. From Fig. 5, it can be seen that d_{33} increases and then decreases with the increase of Sm doping. Meanwhile, ε keeps increasing while P_r and E_c keep decreasing. It seems that with the increase of Sm doping, the trend of d_{33} is firstly determined by the change of ε. When Sm doping exceeds 2.75 mol%, the trend of d_{33} turns to be dominated by the decrease of P_r and E_c. The variations of ε, P_r and E_c may be attributed to the effect of Sm doping on the MPB position[10] (as we have shown in Fig. 3), which further influence the d_{33}. Specifically, the addition of Sm in PMN-PT creates perturbations in the local order parameters such as polarization and strain, leading to heterogeneous polar regions and additional interfacial energies, this leads to a more flattened average free-energy profile for the entire Sm-doped PMN-PT system. Since the reciprocal of the dielectric constant is equal to the second-order derivative of the free energy curve with respect to the independent variable, the flatter the free energy curve is, implying that the smaller the curvature and the second-order derivative, the larger the dielectric constant will be. Different MPB positions imply a different number of possible crystal orientations, thus affecting P_r. This also changes the difficulty of lattice deformation and domain switching, which affects E_c.

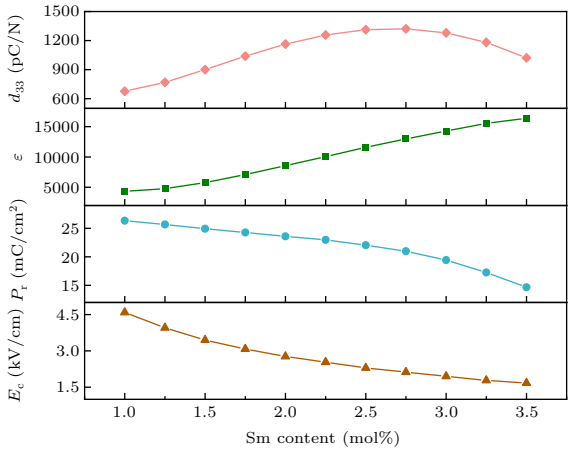


Fig. 5. The d_{33} with ε, E_c, P_r at MPB of PMN-PT ceramics with different Sm doping amounts.

3.4. Database for finding the optimal components quickly

By machine learning, the d_{33} and T_c of Sm-doped PMN-PT ceramics with detailed components in the intervals around MPB positions were obtained. We have organized this huge amount of data into a database so that we can quickly find the optimal components of Sm-doped PMN-PT ceramics according to the different requirements for d_{33} and T_c. The database is openly available in Science Data Bank at https://doi.org/10.57760/sciencedb.j00113.00106. In the following, we pick up the optimal components with the largest d_{33} for Curie temperature intervals spaced at 10 °C from our database. The results are shown in Fig. 6. It is generally recognized that a higher Curie temperature leads to a lower piezoelectric coefficient. However, according to Fig. 6, this rule is broken in the intervals 55 °C to 75 °C and 135 °C to

155 °C. Components within these two intervals may be considered to perform poorly. As an application, if we need to prepare Sm-doped PMN-PT ceramics with a Curie temperature less than 100 °C, the optimal component 2.25 mol% Sm-doped PMN–29.8%PT can be found quickly by Fig. 6. Meanwhile, the piezoelectric coefficient is expected to be up to around 1200 pC/N. In addition to this, it is worth noting that this database also allows us to pick up optimal components according to other different needs.

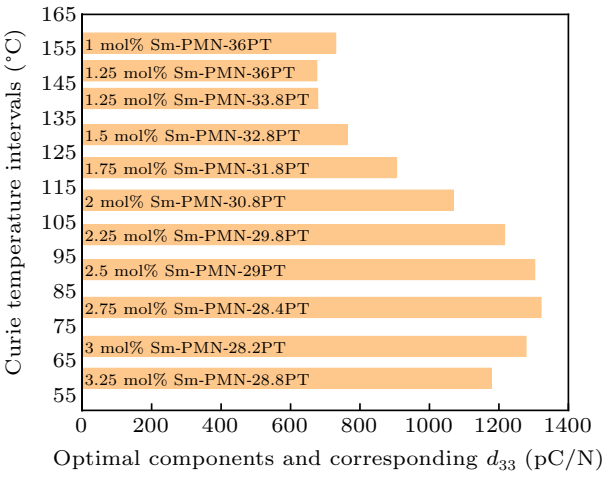


Fig. 6. Optimal components of Sm-doped PMN-PT ceramics and the corresponding piezoelectric coefficients in different Curie temperature intervals.

4. Conclusion and perspectives

In conclusion, we obtained the piezoelectric coefficient and Curie temperature of Sm-doped PMN-PT piezoelectric ceramics with very detailed components by physics-embedded machine learning. It is found that the MPB peak moves in the direction of decreasing PT content with increasing Sm doping amount. The component with the best piezoelectric property is 2.75 mol% Sm-doped PMN–28.4%PT (about 1321 pC/N). In this case, 2.5 mol% Sm-doped PMN–28.4%PT sacrifices some of its piezoelectric property for a higher Curie temperature, and is also considered to have the same excellent comprehensive performance. In addition to this, we set up a database based on model outputs, through which we can quickly find the optimal components of Sm-doped PMN-PT piezoelectric ceramics according to our specific needs. The method proposed in this paper provides a new theoretical idea for predicting the properties of ferroelectric materials. We expect this method will contribute to the development of other ferroelectric materials in the future as well.

Data availability statement

The data that support the findings of this study are openly available in Science Data Bank at the following link https://doi.org/10.57760/sciencedb.j00113.00106

Acknowledgments

Project supported by the National Natural Science Foundation of China (Grant Nos. 52272116 and 12002400), the Natural Science Foundation of Shandong Province (Grant No. ZR2021ME096), and the Youth Innovation Team Project of Shandong Provincial Education Department (Grant No. 2019KJJ012).

References

[1] Cao Y S, Li J R, Sha A M, Liu Z Z, Zhang F and Li X Z 2022 *J. Cleaner Prod.* **369** 133287
[2] Lu J L, Hu S M, Li W R, Wang X F, Mo X W, Gong X T, Liu H, Luo W, Dong W, Sima C, Wang Y J, Yang G, Luo J T, Jiang S L, Shi Z J and Zhang G Z 2022 *ACS Nano* **16** 3744
[3] Christensen-Jeffries K, Couture O, Dayton P A, Eldar Y C, Hynynen K, Kiessling F, O'Reilly M, Pinton G F, Schmitz G, Tang M X, Tanter M and Van S R J G 2020 *Ultrasound Med. Biol.* **46** 865
[4] Trolier-McKinstry S, Zhang S J, Bell A J and Tan X L 2018 *Annu. Rev. Mater. Res.* **48** 191
[5] Wang J J, Wang S H, Li X, Li L, Liu Z, Zhang J and Wang Y J 2023 *J. Adv. Ceram.* **12** 792
[6] Wang F F, Wang H N, Yang Q S, Zhang Z X and Yan K 2021 *Ceram. Int.* **47** 15005
[7] Yang S, Wang M W, Wang L, Liu J F, Wu J, Li J L, Gao X Y, Chang Y F, Xu Z and Li F 2022 *J. Am. Ceram. Soc.* **105** 3322
[8] Li T Y, Liu C, Shi P, Liu X, Kang R R, Long C B, Wu M, Cheng S D, Mi S B, Xia Y H, Li L L, Wang D and Lou X J 2022 *Adv. Funct. Mater.* **32** 2202307
[9] Li F, Lin D B, Chen Z B, Cheng Z X, Wang J L, Li C C, Xu Z, Huang Q W, Liao X Z, Chen L Q, Shrout T R and Zhang S J 2018 *Nat. Mater.* **17** 349
[10] Guo Q H, Hou L T, Li F, Xia F Q, Wang P B, Hao H, Sun H J, Liu H X and Zhang S J 2019 *J. Am. Ceram. Soc.* **102** 7428
[11] Fang Z, Tian X, Zheng F J, Jiang X D, Ye W N, Qin Y L, Wang X X and Zhang Y C 2022 *Ceram. Int.* **48** 7550
[12] Xu B, Kang G Z, Kan Q H, Yu C and Xie X 2020 *Int. J. Mech. Sci.* **168** 105303
[13] Bui T Q and Hu X F 2021 *Eng. Fract. Mech.* **248** 107705
[14] Chen L Q and Zhao Y H 2022 *Prog. Mater. Sci.* **124** 100868
[15] Li F, Cabral M J, Xu B, Cheng Z X, Dickey E C, LeBeau J M, Wang J L, Luo J, Taylor S, Hackenberger W, Bellaiche L, Xu Z, Chen L Q, Shrout T R and Zhang S J 2019 *Science* **364** 264
[16] Batra R, Song L and Ramprasad R 2021 *Nat. Rev. Mater.* **6** 655
[17] Yuan R H, Xue D Q, Xu Y Y, Xue D Z and Li J S 2022 *J. Alloys Compd.* **908** 164468
[18] Yuan R H, Xue D Z, Xue D Q, Zhou Y M, Ding X D, Sun J and Lookman T 2019 *IEEE Trans. Ultrason. Ferroelectr. Freq. Control* **66** 394
[19] Yuan R H, Tian Y, Xue D Z, Xue D Q, Zhou Y M, Ding X D, Sun J and Lookman T 2019 *Adv. Sci.* **6** 1901395
[20] Xu P C, Ji X B, Li M J and Lu W C 2023 *npj Comput. Mater.* **9** 42
[21] Childs C M and Washburn N R 2019 *MRS Commun.* **9** 806
[22] Xue T J, Gan Z T, Liao S H and Cao J 2022 *npj Comput. Mater.* **8** 201
[23] Li C C, Xu B, Lin D B, Zhang S J, Bellaiche L, Shrout T R and Li F 2020 *Phys. Rev. B* **101** 140102
[24] Zheng F J, Tian X, Fang Z, Lin J F, Lu Y, Gao W, Xin R, Fu D S, Qi Y, Ma Z Z, Ye W N, Qin Y L, Wang X X and Zhang Y C 2023 *ACS Appl. Mater. Interfaces* **15** 7053
[25] Li L, Cheng J S, Cheng Y Y, Han T, Liu Y, Zhou Y, Zhao G H, Zhao Y, Xiong C X, Dong L J and Wang Q 2021 *Adv. Mater.* **33** 2102392
[26] Shin W, Yim J, Bae J, Lee J, Hong S, Kim J, Jeong Y, Kwon D, Koo R, Jung G, Han C, Kim J, Park B, Kwon D and Lee J 2022 *Mater. Horiz.* **9** 1623
[27] Yang L Y, Huang H B, Xi Z Z, Zheng L M, Xu S Q, Tian G, Zhai Y Z, Guo F F, Kong L P, Wang Y G, Lü W M, Yuan L, Zhao M L, Zheng H W and Liu G 2022 *Nat. Commun.* **13** 2444
[28] Qiu C R, Wang B, Zhang N, Zhang S J, Liu J F, Walker D, Wang Y, Tian H, Shrout T R, Xu Z, Chen L Q and Li F 2020 *Nature* **577** 350
[29] Li J L, Qu W B, Daniels J, *et al.* 2023 *Science* **380** 87

[30] Apicella A, Donnarumma F, Isgr'o F and Prevete R 2021 *Neural Networks* **138** 14
[31] Zhang X Y and Liu C A 2023 *J. Econom.* **235** 280
[32] Bejani M M and Ghatee M 2021 *Artif. Intell. Rev.* **54** 6391
[33] Plonsky L and Ghanbar H 2018 *Mod. Lang. J.* **102** 713
[34] Karunasingha D S K 2022 *Inf. Sci.* **585** 609
[35] Hodson T O 2022 *Geosci. Model. Dev.* **15** 5481
[36] Mansournia M A, Waters R, Nazemipour M, Bland M and Altman D G 2021 *Global Epidemiol.* **3** 100045
[37] Gerke O 2020 *Diagnostics* **10** 334
[38] Korkmaz M Ç, Chesneau C and Korkmaz Z S 2021 *Symmetry* **13** 117
[39] Dash S, Pradhan D K, Kumari S, Ravikant, Rahaman M M, Cazorla C, Brajesh K, Kumar A, Thomas, Rack P D and Pradhan D K 2021 *Phys. Rev. B* **104** 224105